



Lysosome-targetable selenium-doped carbon nanodots for in situ scavenging free radicals in living cells and mice

Danling Zhou¹ · Hong Huang² · Junrong Yu¹ · Zuming Hu¹

Received: 24 March 2021 / Accepted: 1 June 2021 / Published online: 7 June 2021

© The Author(s), under exclusive licence to Springer-Verlag GmbH Austria, part of Springer Nature 2021

Abstract

Lysosome-targetable selenium-doped carbon nanodots (Lyso-Se-CDs) that can efficiently scavenge lysosomal •OH in living cells and mice were designed in this research. Se-CDs with redox-responsive fluorescence ($\lambda_{\text{ex}} = 379 \text{ nm}$, $\lambda_{\text{em}} = 471 \text{ nm}$, quantum yield = 7.1%) were initially synthesized from selenocystine by a facile hydrothermal method, followed by the surface modification with morpholine, a lysosome targeting moiety. The as-synthesized Lyso-Se-CDs exhibited excellent colloidal stability, efficient scavenging abilities towards •OH, low biotoxicity, as well as good biocompatibility and lysosome targetability. Due to these desirable properties, Lyso-Se-CDs had been successfully utilized for rescuing cells from elevated lysosomal •OH levels. More importantly, Lyso-Se-CDs efficiently relieved phorbol 12-myristate 13-acetate (PMA) triggered ear inflammation in live mice. These findings reveal that Lyso-Se-CDs are potent candidates for treating •OH-related inflammation.

Keywords Lysosome targeting · Redox responsive · Fluorescent carbon nanodots · Antioxidant · Inflammation

Introduction

Reactive oxygen species (ROS) comprising superoxide anions ($\text{O}_2^{\cdot-}$), hydrogen peroxide (H_2O_2), and hydroxyl radicals (•OH) are a series of highly reactive oxygen-containing species [1–5]. Normally, the production and elimination of ROS are in a delicate balance, and the generated ROS are beneficial to many physiological processes [6]. However, due to some exogenous and/or endogenous stimuli, overproduction and accumulation of ROS may happen [7]. This can overwhelm endogenous protective mechanisms and trigger ROS-mediated injury to biomolecules including proteins, DNAs and lipids, leading to a variety of severe diseases, such as

stroke, diabetes, inflammatory disorders, neurodegenerative diseases, and cancer [8, 9].

Over the past few years, numerous nanomaterial-based antioxidants including ceria nanoparticles (CeO_2) [10, 11], manganese oxide nanoparticles (Mn_3O_4 , MnO_2) [12], polydopamine nanoparticles [13], copper-based nanoparticles [14], metal-organic frameworks [15], graphene oxide [16], etc. [17] have been developed for their therapeutic effects to relieve injury and treat ROS-related diseases. For instance, Qu's group synthesized selenium nanoparticle-graphene oxide hybrid nanomaterials to protect cell components against oxidative stress [16]. Wei and coworkers fabricated Mn_3O_4 nanoparticles for in vivo eliminating cellular •OH and $\text{O}_2^{\cdot-}$ with extraordinary efficiency [12]. Wu et al. fabricated ROS eliminating tissue adhesive nanocomposite based on ceria nanocrystal-modified mesoporous silica nanoparticles for restricting ROS-mediated harmful effects and accelerating wound healing [18]. These antioxidants are useful for preventing oxidative damages from cellular ROS. Considering the extremely high reactivity and short half-life of ROS, it is important to prepare targetable antioxidants for in situ scavenging ROS. Lysosomes as cellular acidic organelles (pH 4.0–6.0) contain more than 50 degradative enzymes and play crucial roles in cellular homeostasis and the regulation of varieties of physiological processes [19]. In fact, lysosomes

This article is part of the Topical Collection on *Nanomaterials for biomedical imaging and targeting*

✉ Hong Huang
huangho17@163.com

✉ Zuming Hu
hzm@dhu.edu.cn

¹ College of Materials Science and Engineering, Donghua University, Shanghai 201620, China

² College of Biological Chemical Sciences and Engineering, Jiaxing University, Jiaxing 314001, China

are prone to be affected by $\bullet\text{OH}$, as it is the most abundant ROS inside lysosomes, where its formation is favored by the richness of labile iron ions and the internal acidic microenvironments [20]. To our knowledge, no antioxidants with lysosome-targetable capability have been reported. Thus, to maintain normal status and function of lysosome, it is of great importance to design efficient methods for precisely clearing overproduced $\bullet\text{OH}$ in the lysosome region.

Carbon nanodots (CDs), a novel type of fluorescent carbonaceous nanomaterials, have received tremendous attention in recent years for their water solubility, high resistance to photobleaching, low biotoxicity, good biocompatibility, and wide applications in biological fields [21–24]. In this work, we demonstrate the design and construction of lysosome-targetable Se-doped carbon nanodots (Lyso-Se-CDs) that significantly scavenge lysosomal $\bullet\text{OH}$ in living cells and mice (Fig. 1). Se-CDs covered with redox-responsive unit ($-\text{C}-\text{Se}$) were initially synthesized from selenocystine by a facile hydrothermal method, followed by the surface modification with morpholine, a lysosome targeting moiety. The as-synthesized Lyso-Se-CDs exhibited excellent colloidal stability, robust scavenging abilities towards $\bullet\text{OH}$, low biotoxicity, as well as good biocompatibility and lysosome targetability. Due to these desirable properties, Lyso-Se-CDs had been successfully utilized for rescuing cells from elevated lysosomal $\bullet\text{OH}$ levels. More impressively, Lyso-Se-CDs efficiently relieved PMA triggered ear inflammation in live mice.

Experimental section

Preparation of Se-CDs

Se-CDs were prepared from selenocystine through a one-pot, facile hydrothermal carbonization method. In brief, 0.1 g selenocystine was dispersed in 40 mL of redistilled water with a pH value of ca. 10 (adjusted by 1 M NaOH solution) under rapid stirring. The alkaline solution was used for facilitating the dissolution of selenocystine. Then, the aqueous dispersion was heated at a controlled temperature of 200 °C for 4 h in a 50-mL Teflon-lined autoclave. The resulting solution with a brown color was sequentially purified by filtration with a 0.22 μm filter membrane, centrifugation at 12,000 g for 15 min, and dialysis through a dialysis membrane (cutoff: 1000 Da). After freeze-drying of the as-purified solution, Se-CD powder can be obtained. CDs without Se atom doping were prepared in a same way.

Preparation of Lyso-Se-CDs

Morpholine was immobilized on the Se-CD surface through covalently EDC/NHS activated process. Typically, 5.0 mL of morpholine solution (2.5 mM) was placed into a flask, followed by the injection of 100 mg EDC and 100 mg NHS, and activated at room temperature for 4 h. Afterwards, 2.0 mL of Se-CD solution (1.0 mg mL^{-1}) was added, reacted for 12 h to give morpholine-modified Se-CDs, namely, Lyso-Se-CDs.

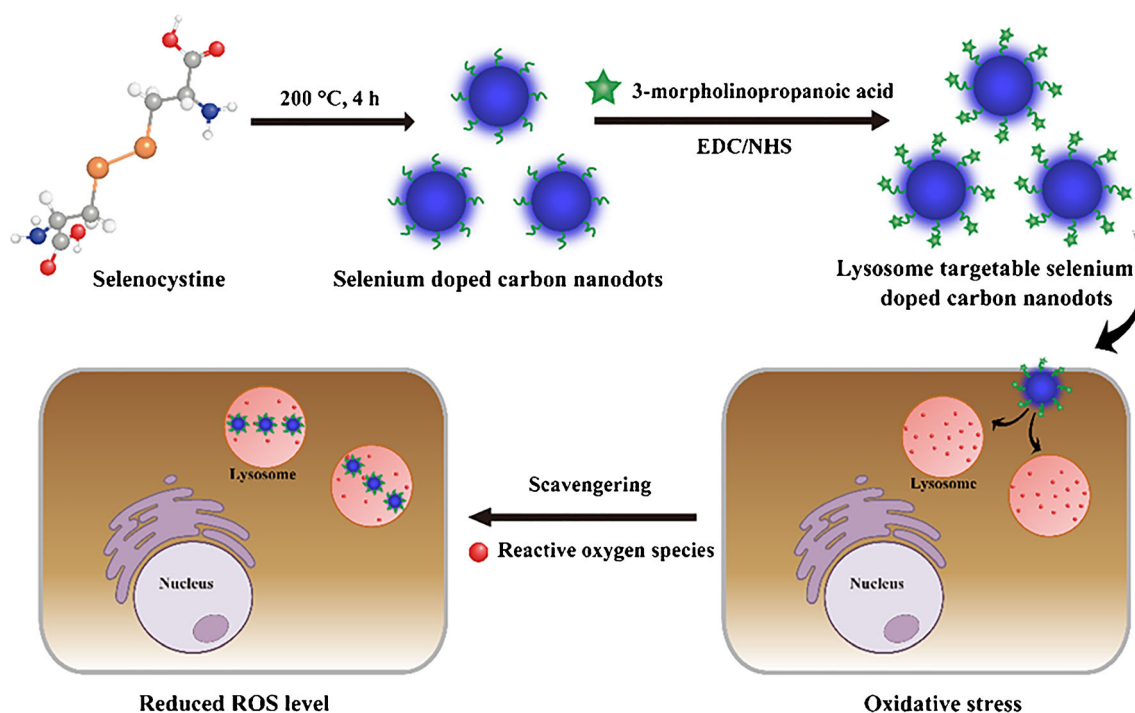


Fig. 1 Schematic illustration of the fabrication of Lyso-Se-CDs and its application in scavenging lysosomal ROS

Cytotoxicity evaluations

HeLa cells were fostered at a density of $\sim 1 \times 10^4$ cells per well in 96-well plates and grown in DMEM containing 10% fetal bovine serum, 80 U mL⁻¹ penicillin, and 80 $\mu\text{g mL}^{-1}$ streptomycin in a humid incubator with 5% CO₂/95% air. After 12 h, the culture media were deserted, and fresh media with serial amounts of Lyso-Se-CDs (0–100 $\mu\text{g mL}^{-1}$) was introduced, cultured for 48 h. As to each amount, five replicate experiments were performed in parallel. Thereafter, MTT solution (1.0 mg mL⁻¹, 20 μL) was injected into each well, waiting for 4 h to allow the generation of formazan crystals. Subsequently, DMSO with a volume of 150 μL was introduced into the wells. Absorbance (A) of the resulting hybrid was determined. The cellular viability values were evaluated by the following equation: cellular viability (%) = $A_{\text{test}}/A_{\text{control}} \times 100\%$, where A_{control} represents the absorbance recorded from the control group, and A_{test} represents the absorbance obtained in the existence of Lyso-Se-CDs.

Fluorescent imaging

Before conducting confocal imaging experiments, HeLa cells were detached, replanted onto confocal dishes (diameter: 35 mm), and adhered for ca. 12 h. Then, the medium in the dish was changed by new one containing Lyso-Se-CDs (20 $\mu\text{g mL}^{-1}$) and cultured for 4 h. Subsequently, the Lyso-Se-CDs labeled HeLa cells were further labeled with LysoTracker Deep Red (100 nM) for 0.5 h. After finishing the above experiments, the labeled cells were rinsed three times with PBS. Under the excitation of 405 nm, the fluorescence image of Lyso-Se-CDs was acquired within 430–510 nm wavelength region, whereas for LysoTracker Deep Red, a 638-nm semiconductor laser was used, and the fluorescence signal was obtained in the wavelength range of 640–720 nm.

All the animal experiments were conducted with the approval of the Animals Ethics Committee of East China Normal University. Kunming mice with a body weight about 15 g were randomly divided into four groups (three mice in each group). The mice in group one, acting as the control group, were subcutaneously injected with 2',7'-dichlorofluorescein diacetate (DCFH-DA, 1 mM, 50 μL) on the right ear. While for the other three groups, PMA acetone solution (100 $\mu\text{g mL}^{-1}$, 50 μL) was topically applied on the right ear to establish an ear inflammation model. After 6 h, the mice were anesthetized using chloral hydrate solution and subcutaneously administered with DCFH-DA (1 mM, 50 μL) or Lyso-Se-CDs (20 $\mu\text{g mL}^{-1}$, 100 μL ; 40 $\mu\text{g mL}^{-1}$, 100 μL) and DCFH-DA (1 mM, 50 μL). After another 0.5 h, fluorescent images of the whole body were acquired on an in vivo imaging system (PerkinElmer) with appropriate wavelength ($\lambda_{\text{ex}} = 488 \text{ nm}$; $\lambda_{\text{em}} = 520 \text{ nm}$).

Results and discussion

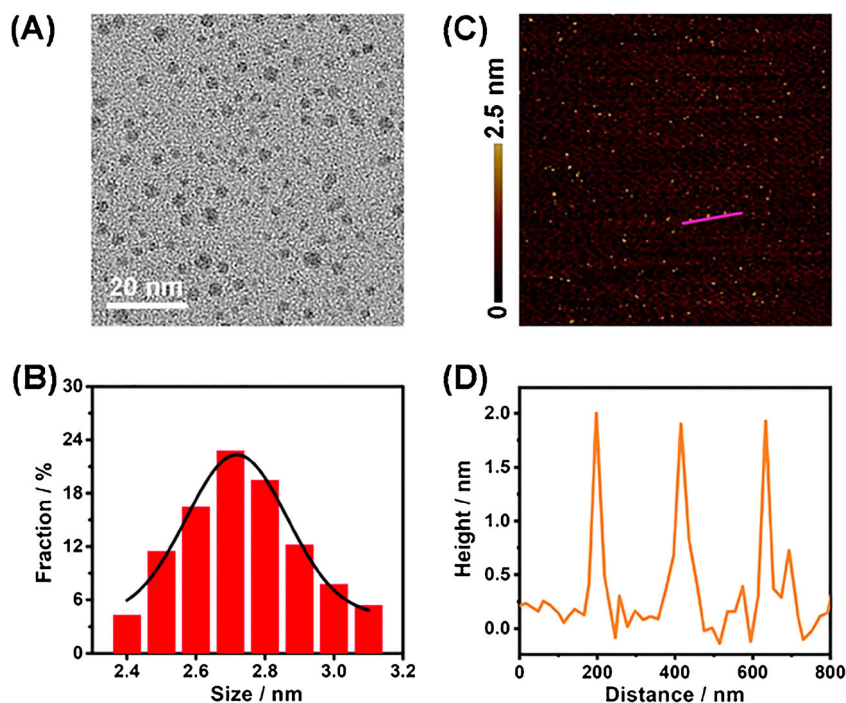
Preparation and characterization of Se-CDs

Inspired by the pioneering work reported by Xu and co-workers [25], Se-CDs were initially prepared in our research through a facile hydrothermal method. Briefly, selenocystine was dissolved in an alkaline solution, treated at 200 °C for 4 h, and water soluble Se-CDs can thus be formed. Morphological characterizations of the synthesized Se-CDs were conducted. TEM image in Fig. 2A demonstrates that the Se-CDs are randomly and uniformly distributed, having a finite size distribution in 2.4–3.1 nm range with a mean value of 2.7 nm, as judged from ca. 100 individual particles (Fig. 2B). This size is much smaller in comparison with the Se-CDs reported by Xu [25] and Huang [26]. Moreover, no assembled larger nanoparticles were observed from our Se-CDs, which suggests that the developed protocol had a good control on size. From AFM image in Fig. 2C, we can find that the Se-CDs were mono-dispersed, showing a height of 2.0 nm (Fig. 2D). This result matched well with TEM characterization.

Then, XPS experiments were performed to analyze the surface states of the Se-CDs. As depicted in Fig. S1A, four predominant peaks were found at 529.6 eV (O_{1s}), 400.9 eV (N_{1s}), 284.5 eV (C_{1s}), along with 55.2 eV (Se_{3d}), testifying the Se-CDs were made up of oxygen, nitrogen, carbon, and selenium, with the atomic ratio of 10.48%, 21.23%, 63.07%, and 5.22%, respectively [27–29]. Specifically, peak deconvolution of the C_{1s} spectrum generates three peaks at 287.9, 286.1, and 284.7 eV, which are corresponded to C=O, C–O/C–N/C–Se, and C–C groups, respectively (Fig. S1B) [30]. The high-resolution XPS spectrum of N_{1s} can be deconvoluted to two peaks at 401.2 and 399.6 eV, attributed to amino N and C–N–C, respectively (Fig. S1C) [31]. The high-resolution XPS spectrum of Se_{3d} (55.2 eV) demonstrates the existence of –C–Se group (Fig. S1D) [32]. In addition, the FTIR spectrum was also determined to investigate the functional groups existed on the surface of Se-CDs (Fig. S2, curve a). The intense absorption band appeared at 3347 cm⁻¹ is attributed to the characteristic stretching vibrations of O–H and N–H [33]. And the absorption peaks at 1570 and 1693 cm⁻¹ is respectively assigned to the C=O stretching vibration of the carbonyl group and N–H [34]. The FTIR data indicated the abundance of –COOH, –OH, and NH₂ groups on Se-CDs surface, which is beneficial to its dispersion in aqueous media and the following surface functionalization.

The fluorescent properties of the Se-CDs were subsequently measured. As depicted, under the excitation with a maximum wavelength at 379 nm (Fig. S3A, curve a), an intense emission peak at 471 nm is observed (Fig. S3A, curve b). The emission peak undergoes a hypsochromic shift compared to that of the Se-CDs reported by Xu [25], with a peak position at 490 nm. The differences between the emission position

Fig. 2 (A) TEM image of the obtained Se-CDs. (B) Size distribution of the Se-CDs. (C) Typical AFM image of the Se-CDs. (D) Height distribution of the Se-CDs along the pink line in Fig. 1C



possibly result from the variation in their sizes [35, 36]. The quantum yield of the Se-CDs was determined to be 7.1%. Similar to most of previously reported CDs, the Se-CDs presented here exhibited excitation-energy-dependent fluorescence (Fig. S3B) [37, 38].

As the surface of Se-CDs was functionalized with $-C-Se$, a unit that can be easily oxidized by oxidant, and the surface states of CDs are correlated with their fluorescence feature, we expected that the Se-CDs would give off redox-responsive fluorescence. To verify our thoughts, H_2O_2 was added into Se-CD solution, and a dramatical enhancement of its fluorescence was witnessed (Fig. S4, curve b). Concurrently, XPS spectroscopy was utilized to study the states of Se atom in Se-CDs in the presence of H_2O_2 . The oxidation state of Se had been changed and oxidized to selenic acid as expected (Fig. S5A). When glutathione was included in the mixed solution of Se-CDs and H_2O_2 , selenic acid could be reduced to $-C-Se$ again (Fig. S5B), associated with the decrease of the fluorescence intensity (Fig. S4, curve c). In parallel, control experiments were also conducted, in which CDs without Se atom doping were prepared, using cystine as the precursor. In this context, no response of the fluorescence of CDs ($\lambda_{em} = 463$ nm) to H_2O_2 was found (Fig. S6). Overall, these results demonstrated that the existence of Se atom and its oxidation state had a quite large impact on the fluorescence emission of Se-CDs.

Synthesis and characterization of Lyso-Se-CDs

For achieving Se-CDs that primarily retained in lysosome, morpholine, an acidotropic group that helps the probe

specifically reside in acidic lysosome via the protonation of the amine unit in acidic milieu [39, 40], was decorated on the Se-CD surface. The decoration of morpholine was implemented through the amidation between $-COOH$ group of 3-morpholinopropanoic acid and $-NH_2$ group of Se-CDs. The covalent conjugation process, activated by EDC/NHS, was characterized by FTIR spectroscopy. 3-morpholinopropanoic acid (Fig. S2, curve b) shows the typical absorption bands of carboxyl group at 3347 cm^{-1} (V_{O-H}) and 1693 cm^{-1} ($V_{C=O}$). The newly generated absorption band at 1612 cm^{-1} in Lyso-Se-CDs spectrum suggests the formation of amide group (Fig. S2, curve c) and the successful anchor of morpholine on the Se-CD surface. Besides, the dynamic light scattering results showed that Lyso-Se-CDs had a larger hydrodynamic size compared to that of Se-CDs, which again proved the attachment of morpholine on the Se-CD surface (Fig. S7).

It is worthy to state that the conjugation of morpholine on the surface of Se-CDs showed no discernible effect on its shape, size (Fig. S8), and fluorescence (Fig. S9). Following, the stability of Lyso-Se-CDs in PBS was analyzed over a period of 7 days. During this period, both the hydrodynamic diameter and fluorescence intensity kept almost constant (Fig. S10), indicative of the high colloidal stability of Lyso-Se-CDs.

ROS scavenging activity of Lyso-Se-CDs

The presence of redox-responsive unit $-C-Se$ on the Lyso-Se-CDs surface suggested its potential usage for eliminating $\cdot OH$, the most reactive ROS. For analyzing

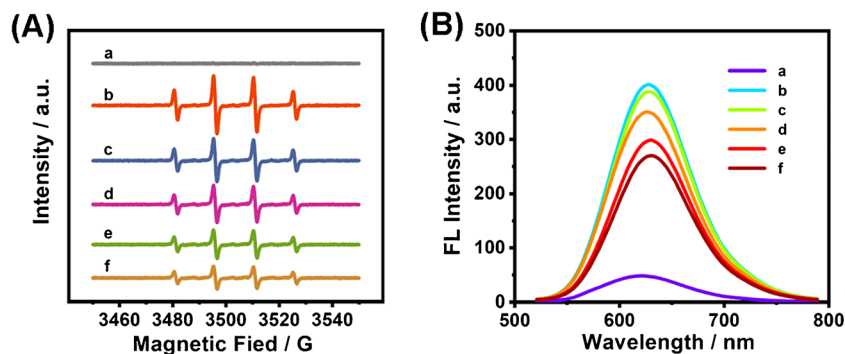


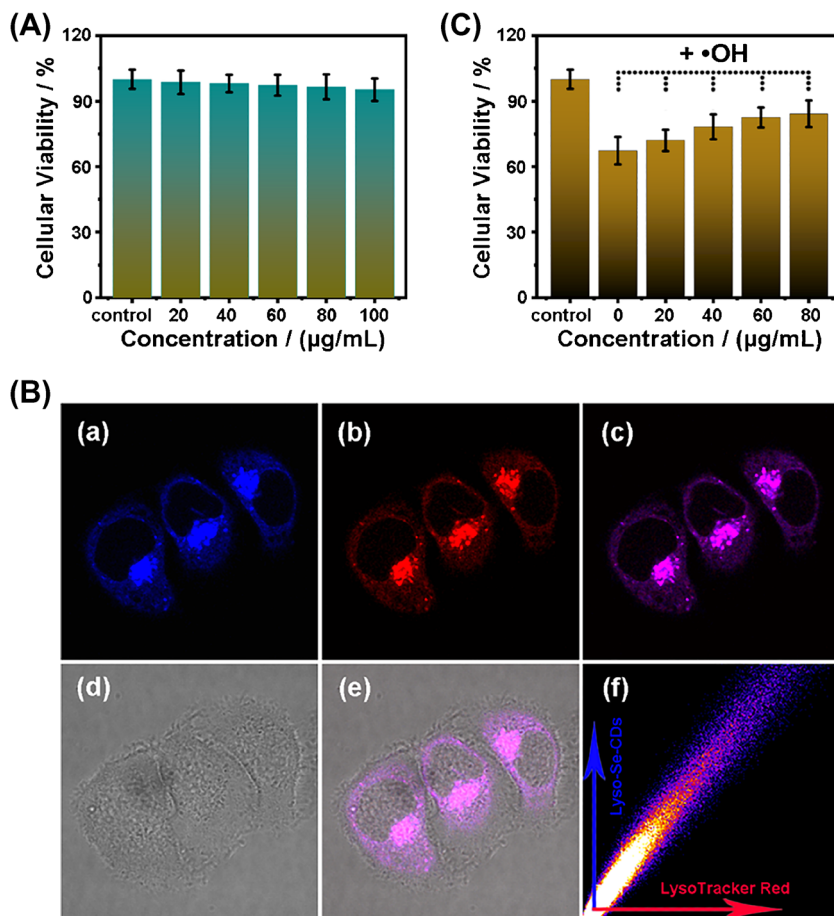
Fig. 3 (A) EPR spectra of DMPO under different experimental conditions. Curve a: DMPO alone; curve b: DMPO + $\bullet\text{OH}$ (10 μM); curve c: DMPO + $\bullet\text{OH}$ (10 μM) + Lyso-Se-CDs (10 $\mu\text{g mL}^{-1}$); curve d: DMPO + $\bullet\text{OH}$ (10 μM) + Lyso-Se-CDs (20 $\mu\text{g mL}^{-1}$); curve e: DMPO + $\bullet\text{OH}$ (10 μM) + Lyso-Se-CDs (30 $\mu\text{g mL}^{-1}$); curve f: DMPO + $\bullet\text{OH}$ (10 μM) + Lyso-Se-CDs (40 $\mu\text{g mL}^{-1}$). The concentration of DMPO was 50 mM. (B) Fluorescence spectra of hydroethidine under

various treatments. Curve a: hydroethidine alone; curve b: hydroethidine + $\text{O}_2^{\bullet-}$ (10 μM); curve c: hydroethidine + $\text{O}_2^{\bullet-}$ (10 μM) + Lyso-Se-CDs (10 $\mu\text{g mL}^{-1}$); curve d: hydroethidine + $\text{O}_2^{\bullet-}$ (10 μM) + Lyso-Se-CDs (20 $\mu\text{g mL}^{-1}$); curve e: hydroethidine + $\text{O}_2^{\bullet-}$ (10 μM) + Lyso-Se-CDs (30 $\mu\text{g mL}^{-1}$); curve f: hydroethidine + $\text{O}_2^{\bullet-}$ (10 μM) + Lyso-Se-CDs (40 $\mu\text{g mL}^{-1}$). The concentration of hydroethidine was 2 μM

its scavenging activity towards $\bullet\text{OH}$, EPR experiments, a direct method to detect ROS, were conducted, choosing 5,5-dimethyl-1-pyrroline N-oxide (DMPO) as the spin trap agent. In the following experiments, $\text{Fe}^{2+}/\text{H}_2\text{O}_2$, the classical Fenton reaction system, was served as the source

to afford $\bullet\text{OH}$. As seen in Fig. 3A (curve a), DMPO molecule showed no EPR signal. Once $\bullet\text{OH}$ was injected to the DMPO solution, a characteristic EPR signal of DMPO-OH adduct appeared, with a 1:2:2:1 quarter pattern (Fig. 3A, curve b) [41]. Gladly, as anticipated, the

Fig. 4 (A) Viabilities of HeLa cells incubated for 48 h with series amounts of Lyso-Se-CDs. (B) Subcellular localization investigations in HeLa cells that were counterstained with Lyso-Se-CDs and LysoTracker Deep Red: a: blue fluorescence from Lyso-Se-CDs ($\lambda_{\text{em}} = 430\text{--}510$ nm); b: red fluorescence from LysoTracker Deep Red ($\lambda_{\text{em}} = 640\text{--}720$ nm); c: the merged image of a with b; d: bright-field image; e: the merged image of c with d; f: the emission correlation plot of the blue channel with red channel. (C) Protective power of Lyso-Se-CDs to HeLa cells against oxidative injury induced by $\bullet\text{OH}$ (100 μM). Data shown are average values, and standard deviations (error bars) are obtained from five independent experiments



introduction of Lyso-Se-CDs weakened the EPR intensity in a dose-dependent manner (Fig. 3A, curve c–f; Fig. S11A). The intensity of EPR signal decreased to 40.7%, with the existence of Lyso-Se-CDs at concentration of $40 \mu\text{g mL}^{-1}$, reflecting the strong $\bullet\text{OH}$ scavenging power of Lyso-Se-CDs. Fluorescence assays further manifested a sensitive response of Lyso-Se-CDs to $\bullet\text{OH}$ (Fig. S12). Moreover, Lyso-Se-CDs also showed an excellent scavenging capacity towards $\text{O}_2^{\bullet-}$ (Fig. 3B; Fig. S11B). Notably, the scavenging behavior of Lyso-Se-CDs is very similar to that of Se-CDs (Fig. S13), disclosing that conjugation of morpholine on the Se-CD surface had no recognizable influence on its antioxidant capacity.

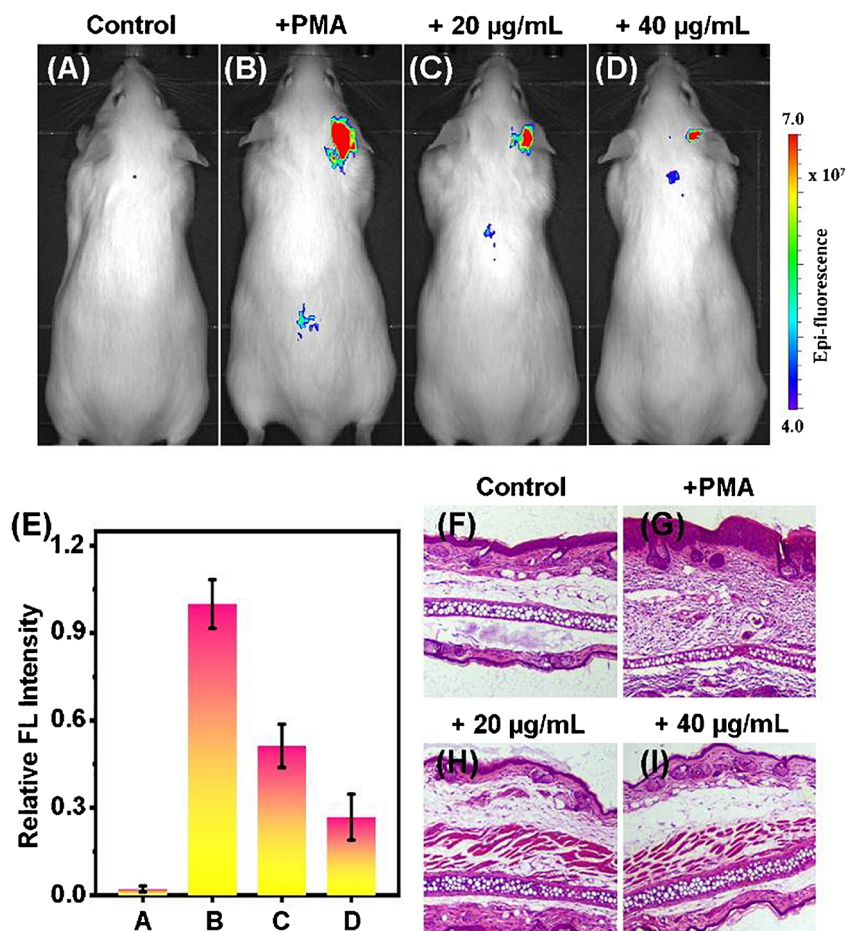
Intracellular $\bullet\text{OH}$ scavenging activity of Lyso-Se-CDs

After in vitro affirming the scavenging ability of Lyso-Se-CDs against $\bullet\text{OH}$, then, its feasibility to scavenging intracellular $\bullet\text{OH}$ was tested. As such, the biotoxicity of Lyso-Se-CDs was checked by MTT assay, in which HeLa cells were treated for 48 h with varied concentrations of Lyso-Se-CDs. As illustrated in Fig. 4A, Lyso-Se-CDs still

exerted feeble side-effects on cellular viabilities even at a concentration up to $100 \mu\text{g mL}^{-1}$, with a value over 90%, denoting low biotoxicity of the Lyso-Se-CDs. Additionally, flow cytometry experiments were also performed (Fig. S14). And the data showed that Lyso-Se-CDs had a good biocompatibility.

Due to Lyso-Se-CDs were engineered with morpholine, its intracellular localization to lysosome was then explored by confocal microscopy experiments. To do so, HeLa cells pretreated with Lyso-Se-CDs were counterstained with LysoTracker Deep Red, a commercial lysosome marker. Figure 4B shows the corresponding fluorescence images of HeLa cells counterstained with Lyso-Se-CDs and LysoTracker Deep Red. The subcellular location of the blue fluorescence signal from Lyso-Se-CDs (Fig. 4Ba) and the deep red emission from LysoTracker Deep Red (Fig. 4Bb) were compared. We can easily find that a large degree of overlap exists between the two images, as visualized from the bright pink signals in Fig. 4Bc, the merged image. Moreover, the intensity correlation plot analysis shows Pearson's coefficient with a high value of 0.91 (Fig. 4Bf). These observations, together, solidly demonstrate that Lyso-

Fig. 5 (A) In vivo fluorescence imaging of mice treated with DCFH-DA (1 mM, 50 μL) alone in the right ear region. (B) In vivo fluorescence imaging of mice sequentially treated with PMA ($100 \mu\text{g mL}^{-1}$, 50 μL) and DCFH-DA (1 mM, 50 μL). (C) In vivo fluorescence imaging of mice treated with PMA ($100 \mu\text{g mL}^{-1}$, 50 μL), Lyso-Se-CDs ($20 \mu\text{g mL}^{-1}$, 100 μL), and DCFH-DA (1 mM, 50 μL) in order. (D) In vivo fluorescence imaging of mice treated with PMA ($100 \mu\text{g mL}^{-1}$, 50 μL), Lyso-Se-CDs ($40 \mu\text{g mL}^{-1}$, 100 μL), and DCFH-DA (1 mM, 50 μL) in order. (E) Relative fluorescence intensity in panel A–D. All the fluorescence intensities were compared to panel B, which was normalized to 1.0. (F–I) Corresponding HE stained images in panel A–D



Se-CDs, with morpholine grafted on surface, specifically reside in lysosome.

In biosystems, oxidative stress happens when the production of ROS surpasses the antioxidant capability of cellular antioxidants, resulting in severe damage to lipids, proteins, and nucleic acids. Since Lyso-Se-CDs exhibited remarkable •OH-scavenging ability, low biotoxicity, as well as good biocompatibility and lysosome targetability, we investigated if Lyso-Se-CDs could suppress oxidative damage from •OH within the lysosome matrix. Here, the $\text{Fe}^{2+}/\text{H}_2\text{O}_2$ system was selected as an injury model to evaluate the protection capability of Lyso-Se-CDs from oxidative stress. The results are presented in Fig. 4C. It was evident that Lyso-Se-CDs, the first antioxidant with lysosome targeting capacity (Table S1), could dose-dependently inhibit •OH-induced decline of cell viabilities.

In vivo anti-inflammation

We further studied the in vivo anti-inflammation behavior of Lyso-Se-CDs. In the experiments, an ear inflammation model was established via topical application of PMA, an apoptotic drug that initiates cell and/or tissue inflammation [42]. As shown in the control mouse (treated with DCFH-DA alone), no obvious fluorescence was observed from the right ear (Fig. 5A), suggesting a low level of ROS. By contrast, an intense fluorescence was observed from the ear treated with DCFH-DA and PMA, revealing the elevated level of ROS in this process (Fig. 5B). After subcutaneous treatment with Lyso-Se-CDs, the fluorescence in the inflamed ear drastically decreased (Fig. 5C, D, and E). Hematoxylin and eosin (HE) stained images of ears were also captured. As displayed in Fig. 5G, lymphocyte infiltration was obviously observed from the slice obtained from PMA-treated mouse, in sharp contrast to the control group (the healthy mouse, Fig. 5F). When further treated with Lyso-Se-CDs, the symptom was attenuated (Fig. 5H, I). All these results suggested that the Lyso-Se-CDs with low biotoxicity and good biocompatibility possessed efficient ROS scavenging ability against ear inflammation.

Conclusions

In conclusion, in this work, we reported the design and construction of Lyso-Se-CDs that can significantly diminish lysosomal •OH in living cells and mice. Further studies revealed that the Lyso-Se-CDs exhibited excellent colloidal stability, robust scavenging abilities towards •OH, low biotoxicity, as well as good biocompatibility and lysosome targetability. Due to these desirable properties, Lyso-Se-CDs had been applied to protect cells from elevated lysosomal •OH levels. More

impressively, Lyso-Se-CDs efficiently relieved PMA triggered ear inflammation in live mice. These findings reveal Lyso-Se-CDs are potent candidates for treating •OH-related inflammation and their potential applications in the fields of biology and medicine.

Supplementary Information The online version contains supplementary material available at <https://doi.org/10.1007/s00604-021-04883-1>.

Funding The authors gratefully thank the Zhejiang Provincial Natural Science Foundation of China (Grant No. LQ20B050003) and Grant from the Scientific Research Start-up Project Foundation of Jiaxing University (CD70519012).

Declarations

Conflict of interest The authors declare no competing interests.

References

- Hou J-T, Yu K-K, Sunwoo K, Kim WY, Koo S, Wang J, Ren WX, Wang S, Yu X-Q, Kim JS (2020) Fluorescent imaging of reactive oxygen and nitrogen species associated with pathophysiological processes. *Chem* 6:832–866
- Li H, Ma H (2018) New progress in spectroscopic probes for reactive oxygen species. *J Anal Test* 2:2–19
- Zhen X, Pu K (2018) Development of optical nanoprobe for molecular imaging of reactive oxygen and nitrogen species. *Nano Res* 11:5258–5280
- Huang H, Tian Y (2018) A ratiometric fluorescent probe for bioimaging and biosensing of HBrO in mitochondria upon oxidative stress. *Chem Commun* 54:12198–12201
- Liu Z, Tian Y (2021) Recent advances in development of devices and probes for sensing and imaging in the brain. *Sci China Chem*. <https://doi.org/10.1007/s11426>
- Kowaltowski AJ, De Souza-Pinto NC, Castilho RF, Vercesi AE (2009) Mitochondria and reactive oxygen species. *Free Radic Biol Med* 47:333–343
- Valko M, Izakovic M, Mazur M, Rhodes CJ, Telser J (2004) Role of oxygen radicals in DNA damage and cancer incidence. *Mol Cell Biochem* 266:37–56
- Valko M, Leibfritz D, Moncol J, Cronin MTD, Mazur M, Telser J (2007) Free radicals and antioxidants in normal physiological functions and human disease. *Int J Biochem Cell Biol* 39:44–84
- Markesbery WR, Carney JM (1999) Oxidative alterations in Alzheimer's disease. *Brain Pathol* 9:133
- Kwon HJ, Cha M-Y, Kim D, Kim DK, Soh M, Shin K, Hyeon T, Mook-Jung I (2016) Mitochondria-targeting ceria nanoparticles as antioxidants for Alzheimer's disease. *ACS Nano* 10:2860–2870
- Kwon HJ, Kim D, Seo K, Kim YG, Han SI, Kang T, Soh M, Hyeon T (2018) Ceria nanoparticle systems for selective scavenging of mitochondrial, intracellular, and extracellular reactive oxygen species in Parkinson's disease. *Angew Chem Int Ed* 57:9408–9412
- Yao J, Cheng Y, Zhou M, Zhao S, Lin S, Wang X, Wu J, Li S, Wei H (2018) ROS scavenging Mn_3O_4 nanozymes for in vivo anti-inflammation. *Chem Sci* 9:2927–2933
- Bao X, Zhao J, Sun J, Hu M, Yang X (2018) Polydopamine nanoparticles as efficient scavengers for reactive oxygen species in periodontal disease. *ACS Nano* 12:8882–8892

14. Liu T, Xiao B, Xiang F, Tan J, Chen Z, Zhang X, Wu C, Mao Z, Luo G, Chen X, Deng J (2020) Ultrasmall copper-based nanoparticles for reactive oxygen species scavenging and alleviation of inflammation related diseases. *Nat Commun* 11:2788
15. Li H, Cao X, Fei X, Zhang S, Xian Y (2019) Nanoscaled luminescent terbium metal–organic frameworks for measuring and scavenging reactive oxygen species in living cells. *J Mater Chem B* 7:3027–3033
16. Huang Y, Liu C, Pu F, Liu Z, Ren J, Qu X (2017) A GO-Se nanocomposite as an antioxidant nanozyme for cytoprotection. *Chem Commun* 53:3082–3085
17. Liu Y, Cheng Y, Zhang H, Zhou M, Yu Y, Lin S, Jiang B, Zhao X, Miao L, Wei C-W, Liu Q, Lin Y-W, Du Y, Butch CJ, Wei H (2020) Integrated cascade nanozyme catalyzes in vivo ROS scavenging for anti-inflammatory therapy. *Sci Adv* 6:eabb2695
18. Wu H, Li F, Wang S, Lu J, Li J, Du Y, Sun X, Chen X, Gao J, Ling D (2018) Ceria nanocrystals decorated mesoporous silica nanoparticle based ROS-scavenging tissue adhesive for highly efficient regenerative wound healing. *Biomaterials* 151:66–77
19. Wu Y, Huang W, Peng D, Huang X-A, Gu J, Wu S, Deng T, Liu F (2021) Synthesis of dihydroquinolines as scaffolds for fluorescence sensing of hydroxyl radical. *Org Lett* 23:135–139
20. Benitez-Martin C, Guadix JA, Pearson JR, Najera F, Perez-Pomares JM, Perez-Inestrosa E (2019) A turn-on two-photon fluorescent probe for detecting lysosomal hydroxyl radicals in living cells. *Sensors Actuators B Chem* 284:744–750
21. Li F, Yang D, Xu H (2019) Non-metal-heteroatom-doped carbon dots: synthesis and properties. *Chem Eur J* 25:1165–1176
22. Zhou J, Zhou H, Tang J, Deng S, Yan F, Li W, Qu M (2017) Carbon dots doped with heteroatoms for fluorescent bioimaging: a review. *Microchim Acta* 184:343–368
23. Zhou D, Huang H, Wang Y, Wang Y, Hu Z, Li X (2019) A yellow-emissive carbon nanodot-based ratiometric fluorescent nanosensor for visualization of exogenous and endogenous hydroxyl radicals in the mitochondria of live cells. *J Mater Chem B* 7:3737–3744
24. Liu Z, Pei H, Zhang L, Tian Y (2018) Mitochondria-targeted DNA nanoprobe for real-time imaging and simultaneous quantification of Ca^{2+} and pH in neurons. *ACS Nano* 12:12357–12368
25. Li F, Li T, Sun C, Xia J, Jiao Y, Xu H (2017) Selenium-doped carbon quantum dots for free-radical scavenging. *Angew Chem Int Ed* 56:9910–9914
26. Rosenkrans ZT, Sun T, Jiang D, Chen W, Barnhart TE, Zhang Z, Ferreira CA, Wang X, Engle JW, Huang P, Cai W (2020) Selenium-doped carbon quantum dots act as broad-spectrum antioxidants for acute kidney injury management. *Adv Sci* 7:2000420
27. Su R, Shi J, Pu Y, Wang J-X, Wang D, Chen J-F (2020) Synthesis of ultrasmall and monodisperse selenium-doped carbon dots from amino acids for free radical scavenging. *Ind Eng Chem Res* 59:16876–16883
28. Zhu J-H, Feng Y-G, Wang A-J, Mei L-P, Luo X, Feng J-J (2021) A signal-on photoelectrochemical aptasensor for chloramphenicol assay based on 3D self-supporting AgI/Ag/BiOI Z-scheme heterojunction arrays. *Biosens Bioelectron* 181:113158
29. Shen Z, Cai Q, Yin C, Xia Q, Cheng J, Li X, Wang Y (2020) Facile synthesis of silica nanosheets with hierarchical pore structure and their amine-functionalized composite for enhanced CO_2 capture. *Chem Eng Sci* 217:115528
30. Luo W, Wang Y, Lin F, Liu Y, Gu R, Liu W, Xiao C (2020) Selenium-doped carbon quantum dots efficiently ameliorate secondary spinal cord injury via scavenging reactive oxygen species. *Int J Nanomedicine* 15:10113–10125
31. Ye X, Xiang Y, Wang Q, Li Z, Liu Z (2019) A red emissive two-photon fluorescence probe based on carbon dots for intracellular pH detection. *Small* 15:1901673
32. Huang H, Shen Z, Chen B, Wang X, Xia Q, Ge Z, Wang Y, Li X (2020) Selenium-doped two-photon fluorescent carbon nanodots for in-situ free radical scavenging in mitochondria. *J Colloid Interface Sci* 567:402–409
33. Simões EFC, Leitão JMM, Esteves Da Silva JCG (2017) Sulfur and nitrogen co-doped carbon dots sensors for nitric oxide fluorescence quantification. *Anal Chim Acta* 960:117–122
34. Bauer C, Jacques P, Kalt A (1999) Investigation of the interaction between a sulfonated azo dye (AO7) and a TiO_2 surface. *Chem Phys Lett* 307:397–406
35. Wang Y, Hu A (2014) Carbon quantum dots: synthesis, properties and applications. *J Mater Chem C* 2:6921
36. Li H, He X, Kang Z, Huang H, Liu Y, Liu J, Lian S, Tsang CHA, Yang X, Lee ST (2010) Water-soluble fluorescent carbon quantum dots and photocatalyst design. *Angew Chem* 122:4532–4536
37. Lu S, Sui L, Liu J, Zhu S, Chen A, Jin M, Yang B (2017) Near-infrared photoluminescent polymer–carbon nanodots with two-photon fluorescence. *Adv Mater* 29:1603443
38. Dam BV, Nie H, Ju B, Marino E, Paulusse JMJ, Schall P, Li M, Dohnalová K (2017) Excitation-dependent photoluminescence from single-carbon dots. *Small* 13:1702098
39. Liu H, Sun Y, Li Z, Yang J, Aryee AA, Qu L, Du D, Lin Y (2019) Lysosome-targeted carbon dots for ratiometric imaging of formaldehyde in living cells. *Nanoscale* 11:8458–8463
40. Wang Q, Zhou L, Qiu L, Lu D, Wu Y, Zhang X-B (2015) An efficient ratiometric fluorescent probe for tracking dynamic changes in lysosomal pH. *Analyst* 140:5563–5569
41. Huang H, Lou X, Hu B, Zhou Z, Chen J, Tian Y (2019) A comprehensive study on the generation of reactive oxygen species in Cu-A β -catalyzed redox processes. *Free Radic Biol Med* 135:125–131
42. Wu J, Yu Y, Cheng Y, Cheng C, Zhang Y, Jiang B, Zhao X, Miao L, Wei H (2021) Ligand-dependent activity engineering of glutathione peroxidase-mimicking MIL-47(V) metal–organic framework nanozyme for therapy. *Angew Chem Int Ed* 60:1227–1234

Publisher's note Springer Nature remains neutral with regard to jurisdictional claims in published maps and institutional affiliations.